Alkaline earth-driven structural evolution and dissolution behavior of Cu-doped zinc polyphosphate antibacterial glasses.

GUO, Ruixin, ZHAO, Zhengkun, DENG, Wei, CHAKRABARTI, Anirban, OJOVAN, Michael and XU, Kai

Alkaline Earth-Driven Structural Evolution and Dissolution Behavior of Cu-doped Zinc Polyphosphate Antibacterial Glasses

Ruixin Guo[a], Zhengkun Zhao[a,b], Wei Deng[c], Anirban Chakrabarti[a], Michael Ojovan[a,d], Kai Xu[a,*]

[a] State Key Laboratory of Silicate Materials for Architectures, Wuhan University of Technology, Wuhan 430070, P. R. China

[b] Anhui Zhenghe Materials Technology Co., Ltd, Chuzhou 239000, P. R. China

[c] College of Business, Technology and Engineering, Sheffield Hallam University, City Campus, Sheffield S1 1WB, UK

[d] School of Chemical, Materials and Biological Engineering, The University of Sheffield, Sheffield S10 2TN, UK

[*] Corresponding author

E-mail address: kaixu@whut.edu.cn (K. Xu).

Abstract:

Due to the dissolution-controlled release of Cu^{2+}/Zn^{2+} ions that inactivate bacterial proteins, Cu-doped zinc metaphosphate glasses demonstrate broad-spectrum antibacterial activity. However, the role of alkaline earth oxides (AE) governing dissolution behavior and antibacterial efficacy of Cu-doped zinc phosphate glasses is insufficiently understood. Hence, this study used the traditional melt-quenching method to synthesize glasses with molar compositions of $45P_2O_5$-45ZnO-10AE (AE = MgO, CaO, SrO, or BaO) and 2 mol% CuO doping. As the ionic field strength decreased from Mg^{2+} to Ba^{2+}, the phosphorus-oxygen network was depolymerized, accompanied by improved water resistance and decreased antibacterial activity in 2 h. The improved water resistance could be attributed to the increased crosslink provided by the introduction of AE and the improved structrural stability of Zn-O coordination, as examined via EXAFS analysis, which decreased the release of Cu^{2+}/Zn^{2+} ions. Compared to the uniform dissolution behavior for other glasses, the BaO-containing glass exhibited a selective dissolution behavior and anomalously higher water resistance within 73 d of water immersion. As observed by FE-SEM, this phenomenon was accompanied by the formation of a thin and dense layer on the glass surface, which has rarely been reported for soluble phosphate glasses.

Key words:

Zinc phosphate glass, antibacterial glass, alkaline earth oxides, glass structure, dissolution behavior

1. Introduction

Zinc phosphate glass has attracted vast attention due to the versatility of the glass network, which can accommodate a high content of antibacterial agent Zn^{2+} and release it into aqueous media [1][2]. Zn^{2+} exposure inhibits bacterial growth through multiple mechanisms, such as membrane disruption and protein inactivation, leading to a broad-spectrum antibacterial activity of zinc phosphate glasses [3]. Subsequently, this generates potential applications in various fields, such as medical treatment, food packaging, and contaminated soil/water remediation [2][3][4]. However, zinc phosphate glasses have inevitably limited applications due to their poor chemical durability in aqueous environments [5][6]. For instance, the bulk glass with a molar composition $40P_2O_5$-55ZnO-$1Ga_2O_3$-$4Ag_2O$ had a ~10% weight loss after 3 h of immersion in 50 mL of static deionized water, which potentially degraded the antibacterial efficacy in a short time [7]. Therefore, aqueous durability tuning of zinc phosphate glass must be investigated to achieve long-lasting antibacterial properties.

The aqueous resistance of phosphate glass is strongly correlated with the glass network polymerization, the type of phosphate tetrahedral units determined by the phosphate to modifier molar ratio, and the type of modifier cations present and their field strength [8]. The metaphosphate glass has an O/P molar ratio of exactly three and a glass network consisting of Q^2 units, forming long phosphate chains [9]. The increase in the modifier content decreases the length of these phosphate chains and simultaneously increases the content of nonbridging oxygen (NBO), i.e., terminal oxygen [6]. Notably, the hydration of entire phosphate chains together with the associated cations governs the dissolution of metaphosphate glass [8]. Despite the accumulation of terminal oxygens, glass had significantly enhanced chemical durability due to the incorporation of divalent or multivalent metals, such as Ca^{2+} [10], Zn^{2+} [11], Fe^{3+} [12], and Ti^{4+} [13], into the phosphate glass network since these metal ions had increased ionic crosslinks with the terminal oxygens from the phosphate chains. For instance, the increased x values in the $10Na_2O$-$(20 + x/2)$ZnO-$(20 + x/2)$CaO-$(50 - x)P_2O_5$ ($0 \leq x \leq 20$) glass system drastically enhanced the glass water resistance in

deionized water due to the decreased water ingress and degree of structural openness, which was associated with the increased crosslinks and the decreased concentration of P-O-P linkages [11]. Extensive studies found that replacing a lower field strength cation with a higher one could improve the aqueous durability of glass due to the increased ionic crosslink strength of the phosphate chains from the higher field strength cation [8][14]. Besides, the degree of structural openness and crosslinking of phosphate chains were significantly changed due to the local structure of modifiers, especially in the binary phosphate glass system, like zinc phosphate glasses [11]. This leads to discontinuities in the composition–property behavior of the binary zinc phosphate composition due to the changed [ZnO_4] and [ZnO_6] fraction in the glass structure (e.g., the glass transition temperature goes through a minimum with the increase in ZnO content from the metaphosphate to the pyrophosphate stoichiometry [1][15]).

Practical applications frequently added copper oxide (CuO) into Zn-based antibacterial glasses to broaden the antibacterial activity range and reduce bacteria resistance [2][3]. However, the valence state of the glass-incorporated Cu was susceptible to glass composition and melting temperature. Notably, different Cu forms, including monovalent (Cu^+), divalent (Cu^{2+}), and metallic (Cu^0) particles, determined the release of copper ions, leading to different antibacterial efficacies (e.g., Cu^+ ions have stronger antibacterial activity than Cu^{2+} ions under test conditions that mimic microbial contamination on solid surfaces, while the precise mechanism is unclear) [16]. For example, the molecular dynamics simulations demonstrated the steric constraints surrounding the Cu^+ ions, which limited the ion exchange between the H_3O^+ and Cu^+ ions to result in insufficient release of Cu^+ and decreased antibacterial activity of glass [17]. On the contrary, Cu^0 particles dispersed in the glass matrix could potentially deteriorate the phosphate network since Colomban's work recorded a less polymerized glass network around the Cu^0 particles [18]. However, alkaline earth oxides (AE) were frequently introduced into the phosphate glass system to increase the crosslinks of phosphate tetrahedral units, which potentially impacted the Cu species in the glass due to their different optical basicity [19] and the aqueous durability of glass that determined the antibacterial activity of glass associated with Cu/Zn release capacity. Nevertheless,

the effect of AE on Cu species-structure-aqueous durability of zinc phosphate glass has not been fully understood.

This study investigated the effects of AE on Cu species, Zn local structure, water resistance, and the antibacterial activity of Cu-doped ternary glass P_2O_5-ZnO-AE (AE = MgO, CaO, SrO, or BaO). The oxidation states of Cu as the addition of different AE was identified using Ultraviolet-visible (UV-vis) spectrophotometry and powder X-ray diffraction (XRD) detected the presence of metallic Cu. P-O network and Zn-O coordination were revealed using Raman spectrometry, nuclear magnetic resonance (NMR) spectrometry for ^{31}P, and the Zn K-edge extended X-ray absorption fine structure (EXAFS). The glass dissolution behavior was analyzed using the water immersion test, and the element concentration released from the glass was analyzed using inductively coupled plasma atomic emission spectrometry (ICP-AES). The morphological evolutions of post-dissolution glass were characterized using field emission scanning electron microscopy (FE-SEM). The Cu species, structural evolutions, antibacterial activity, and long-term dissolution behavior were discussed as dependent on the addition of different AE.

2. Experimental

2.1. Glass Preparation

The traditional melt-quenching method was used to prepare five glasses with 2.0 mol% CuO (the nominal molar compositions are displayed in Table 1). Analytical grade reagents of $NH_4H_2PO_4$, ZnO, $MgCO_3$, $CaCO_3$, $SrCO_3$, $BaCO_3$, and CuO were used for batch preparation. First, 30 g of the mixed batch was put in a corundum crucible, followed by melting in a box furnace at 1050 °C for 0.5 h. Then, the homogenized melt was poured onto a preheated brass plate, followed by pressing with another plate to form a thin glass sheet. Then, the quenched glasses were polished to 1.0 mm thick glass sheets or ground into fine powders for characterization. The volatilization of P_2O_5, contamination of Al_2O_3, and actual molar ratio of O/P were obtained using the ICP-AES (Leeman Labs, Prodigy 7) as shown in Table 1.

The effect of AE on Cu species in the glass matrix was investigated by re-heating

the as-made glass from room temperature to 1050 °C at a 10 °C/min heating rate, followed by keeping it at 1050 °C for 10 min and cooling in the furnace under N_2 and air, respectively. The ~1 mm thick surface layer of the remelted glasses was cut and polished for optical absorption measurement, followed by grinding into fine powders for characterization.

2.2. Characterizations of Cu species and the properties and structure of glass

2.2.1. Physical properties and Cu species analysis

The density of the glasses was measured using densimetry (Shimadzu AUY120) at ~25 °C, which employed Archimedes principle and the immersion medium was silicone fluid (XIAMETER PMX-200, 1000 CS). The average density was calculated using five repeated measurements of glass samples. The molar volumes V_m (cm^3/mol) of the glasses are obtained from the density measurements as follow:

$$V_m = \frac{X_{P_2O_5}M_{P_2O_5} + X_{ZnO}M_{ZnO} + X_{AE}M_{AE} + X_{CuO}M_{CuO}}{\rho}$$

Where X_{P2O5}, X_{ZnO},… are the molar proportions contributed by the constituent oxides, P_2O_5, ZnO,… to the total oxide content of the glass, M_{P2O5}, M_{ZnO},… are the molar mass of these individual oxides, ρ denotes the density (g/mL) of glass.

To investigate the potential effect of exhaustion of reductive microatmosphere created by the decomposition of the phosphate on the Cu species during glass melting process, the viscosity of the glass melts was measured following the protocol reported in a previous study [20]. A rotating spindle viscometer (Orton RSV1600) with a Pt spindle suspended in the melt at a predetermined depth was used. Approximately 200 g powdered glass was placed in a 150 mL corundum crucible, followed by heating from room temperature to the target temperature (1100 °C) at a heating rate of 10 °C/min. The sample was held at the target temperature for 30 min. Afterward, the spindle was rotated with a constant speed of 80 rpm, as the temperature decreased from the target temperature to 850–950 °C at the decreasing rate of 5 °C/min, and the viscosity spanning from 0 to 7 Pa·s was measured.

The valence states of the Cu species in the glass samples were analyzed using UV-vis spectrophotometry (Shimadzu UV3600). The UV-vis spectra were recorded for

optically polished glass samples in the 200–1200 nm wavelength range. The spectral line jumps at ~710 and ~820 nm were attributed to detector switching and were smoothed using the Savitzky–Golay method. The crystalline phases in the glass samples were identified using powder XRD (Bruker D8 Discovery, Cu Kα radiation, λ = 1.5406 Å) at 40 kV and 40 mA for 2θ = 15–60° at an 8°/min scan rate and a 0.02° step size.

2.2.2. Phosphorus-oxygen structure

The glass structure was analyzed using Raman spectrometry (Horiba LabRam HR Evolution) and solid-state NMR spectrometry (Bruker AVANCE NEO 600WB for ^{31}P). The Raman spectral profiles were recorded for optically polished surfaces of glasses across a 600–1400 cm^{-1} wavelength range with a 532 nm laser. The NMR spectral profiles were recorded for finely ground glass powders from –250 to +200 ppm. The ^{31}P magic-angle spinning-nuclear magnetic resonance (MAS-NMR) spectra were recorded with a 3.2 mm HXY probe corresponding to the 242.95 MHz frequency for ^{31}P (recycle delay = 1024 s, number of scans = 4, 1.047 μs of pulse length corresponding to π/6 flip angle). The rotor was rotated at 20 kHz.

2.2.3. Zn K-edge EXAFS

The local structure of Zn^{2+} ions was analyzed using X-ray absorption spectroscopy (XAS) at the BL14W station in Shanghai Synchrotron Radiation Facility (SSRF), where the storage rings were operated at 3.5 GeV with a 250 mA maximum current. A Lytle detector was used for these measurements in the transmission mode. The samples were pelletized into disks of 8 mm diameter using graphite powder as a binder. The EXAFS spectra were processed following the standard procedures with the ATHENA module of the IFEFFIT software packages. The post-edge background was subtracted from the overall absorption and normalized with respect to the edge jump step to obtain the EXAFS spectra. Then, χ(k) data in the *k*-space range of about 3–10.5 Å^{-1} were Fourier transformed to real (*R*) space using hanning windows (dk = 1.0 Å^{-1}) to separate the EXAFS contributions from different coordination shells. The least-squares curve fitting in the *R*-space with a Fourier transform *k*-space range of 2–11 Å^{-1}, using the ARTEMIS module of the IFEFFIT programs, obtained the quantitative information. The backscattering amplitude (F(k)) and phase shift (Φ(k)) were calculated using the

FEFF8.0 code.

2.3. Antibacterial activity

The antibacterial activities of the glasses were evaluated against *E. coli* (ATCC, 25922) using the quantitative viable count method. *E. coli* was precultured in 3 mL of Luria-Bertani (LB) broth at 37 °C for 15 h while shaking at 200 rpm. The *E. coli* suspension concentration was regulated to 10^7 colony-forming units (CFU)/mL. The antibacterial activity was evaluated by mixing 3 mL of this suspension with 20 mg of glass samples (grain size: 54–75 μm), followed by incubation at 37 °C for 2 h with shaking at 200 rpm. Then, the mixture was diluted 10^5 times, and 0.1 mL of that was inoculated on LB agar plates, followed by incubation at 37 °C for 18 h. The colonies formed were counted to determine the number of viable bacteria. The antibacterial activity was positively correlated with $\log_{10}$ of the reduction of colonies calculated following the literature [17]. The tests were carried out in triplicate.

2.4. Glass dissolution experiment against water

The elemental release and antibacterial activity of the glass samples were examined using the water immersion test. Grains with sizes in the 54–75 μm range were acquired by grinding the glass samples in an agate mortar, followed by sieving through a mesh (size range: –200 to +300). The powders were ultrasonically cleaned with ethanol and dried overnight in an oven at 105 °C. Then, exactly 0.50 g of powders (± 0.5 mg) were placed in a 50 mL sealed Teflon vessel, which was filled with 50 mL of ultrapure water (pH = ~5.6) and was kept in an oven at 37 ± 1 °C for 73 d. A 2 mL leachate was extracted using a pipette for element concentration analysis after 0.08, 0.5, 1, 2, 4, 8, 16, 33, and 73 d. Then, the vessel was replenished with 2 mL of ultrapure water to maintain a constant volume. The extracted leachate was filtered through a 0.45 μm filter, followed by adding a drop of diluted HNO_3 to avoid any precipitates and measuring the concentration of the released elements using ICP-AES. Additionally, the tests were carried out in duplicate.

The morphological evolutions of the post-dissolution glass were revealed by immersing the glass particles from each water immersion experiment after 2, 16, and 50 d, followed by retrieving, cleaning, and drying overnight in an oven at 105 °C. The

dried glass particles were ground gently in an agate mortar to obtain a fresh cross-section of the glass alteration layer. The morphology of the glass alteration layer was examined using FE-SEM (Zeiss Ultra Plus) operated at a 5 kV accelerating voltage. The crystalline phases of the post-dissolution glass samples were identified using XRD in the 5–50° range following the characterizing protocol stated in Section 2.2. The atom% of each element within the top ~5–10 nm of the pre- and post-dissolution glass surfaces was analyzed using X-ray photoelectron spectrometry (XPS, Thermo Scientific K-Alpha) and calculated following the literature [21].

3. Results

3.1. The density and optical absorption

The density of the glass samples increased from ~2.78 to ~2.88 g/cm^3 as 10 mol% MgO was added and increased to ~3.22 g/cm^3 as BaO replaced MgO (Fig. 1). Significantly, the molar volume abruptly decreased from ~39.9 to ~36.1 cm^3/mol when MgO was added, but stayed nearly in the same level as a lower field strength AE replaced MgO.

The images and UV-vis spectra of glass samples are shown in Fig. 2. Although the base glass sample was colorless and transparent, the color of the glasses became opaque red when MgO was added. Subsequently, it gradually became transparent reddish as CaO or SrO substituted MgO. Interestingly, the addition of BaO shifted the color to transparent green. The absorption spectra of all glasses, excluding Mg10, had an absorption edge near 300 nm, which may be attributed to the $3d^{10} \rightarrow 3d^9 4s^1$ transitions of the Cu^+ ions [22][23]. Glasses Ca10 and Sr10 showed absorption bands at ~570 nm, indicating the surface plasmon resonance (SPR) effect of Cu^0 clusters dispersed in the glass matrix [24]. The content of Cu^0 clusters could reach a critical value for facilitating their diffusion and growth during glass preparation, which induced the inhomogeneous red color for glasses Ca10 and Sr10 and was in agreement with Gao's study [25]. The wide absorption band between ~600 and ~1000 nm for glass Ba10, with its center at ~780 nm, contributed to the d-d transitions of Cu^{2+} ions [23][24]. Therefore, it could be assumed that the primary Cu valence states were Cu^+ in the base glass, Cu^+ and Cu^0 in

glasses Ca10 and Sr10, and Cu^{+} and Cu^{2+} in glass Ba10. The intense absorbance near 600 nm for glass Mg10 could be attributed to the high Cu^{0} concentration.

3.2. Glass structure

The Raman spectra analysis (Fig. 3) obtained the data on glass structure, and the Raman band assignments are listed in Table 2. The Raman spectrum of the base glass showed a typical metaphosphate glass pattern. The Raman bands at 702 and 758 cm^{-1} corresponded to the symmetrical stretches of bridging oxygen (BO) in Q^2 and Q^1 units, respectively [15][26]. The bands at 1206 and 1252 cm^{-1} were assigned to the symmetrical and asymmetrical stretches of NBO in Q^2 units, respectively [15][27][28]. The band representing symmetrical stretches in NBO from Q^2 units shifted from 1206 to 1200 cm^{-1} when MgO was added. Furthermore, this band shifted to a lower Raman shift at 1185 cm^{-1} when BaO replaced MgO. Meanwhile, the difference of intensities between the bands at 1206 and 702 cm^{-1} decreased as different AE were added, indicating potential alteration of phosphorus-oxygen tetrahedron units. The introduction of AE increased the intensities of bands representing P-O stretches of Q^1 chain terminator at 1010 and 1138 cm^{-1}, and symmetrical stretches of NBO in Q^1 units at 1048 cm^{-1} [15][26]. The increase indicated the accumulation of terminal oxygen atoms. The spectra of four AE-containing glasses displayed similar Raman patterns, and the structure of the phosphorus-oxygen network was further analyzed using ^{31}P NMR.

Gaussian fittings could deconvolute the ^{31}P NMR spectral profiles of the base glass and AE-containing glasses into two components (Fig. 4), and the fitting parameters are listed in Table 3. The base glass spectrum had two signals centered at −12.4 and −30.7 ppm, which were attributed to Q^1 and Q^2 units, respectively [29][30]. The introduction of AE generally shifted the chemical shifts of these signals to the less negative values, such as −11.0 and −28.2 ppm for the Q^1 and Q^2 units in Ba10, respectively, which deshielded the Q^1 and Q^2 peaks. The deshielding effect correlated with the decreased cationic potential (Z/a, where Z = charge number and a = cation–oxygen distance) and the decreasing covalency of the BO bond as the cationic field strength decreased in AE [31][32]. The proportions of the Q^1 and Q^2 units in the base glass were 10.7% and 89.3%, respectively. The proportions of the Q^1 and Q^2 units increased to 25.9% and decreased

to 74.1% when MgO was added, respectively. Consequently, this indicated that a portion of Q^2 converted into Q^1, depolymerizing the phosphorus-oxygen network and accumulating terminal oxygen atoms. However, Q^2 continued to convert into Q^1 when the other three AE replaced MgO, further depolymerizing the phosphorus-oxygen network. As AE was introduced, the full width at half-maximum (FWHM) of Q^1 units of all glasses increased from 10.2 to 12.4 ppm and then gradually decreased to 10.7 ppm. The FWHM of Q^2 units of glasses increased from 12.9 to 15.0 ppm, indicative of an increased distortion from the phosphorus-oxygen tetrahedron units [32].

3.3. Elemental release and antibacterial activity test

Leaching tests of glasses determined the released concentrations of P, Zn, M, and Cu after 2 h at 37 ± 1 °C, where M represented the alkaline earth metal elements (Fig. 5a). In the base glass, the released concentrations of P, Zn, and Cu were ~1788, ~503, and ~73 ppm, respectively (Fig. 5a). When MgO was added, P, Zn, and Cu from the glasses showed significantly reduced leaching concentrations (> 50%). When BaO replaced MgO, the three elements had 80–90% reduced leaching concentrations compared to the base glass. All elements in each sample had similar levels of normalized concentrations, exhibiting a congruent dissolution behavior for all glasses (Fig. 5b).

The antibacterial activity recorded against *E. coli* in 2 h from all glasses in Fig. 6, indicated the $\log_{10}$ reduction of bacteria. The base glass had > 4-log reduction (> 99.99% reduction), but the antibacterial activity decreased to ~1.5-log reduction (96.47% reduction) when MgO was added. When BaO replaced MgO, it continued decreasing to < 1-log reduction (42.24% reduction).

4. Discussion

4.1. Effect of AE on the Cu species

Glass Ca10 had a higher absorption of Cu^0 at ~570 nm than glass Sr10, indicating that Ca10 had a higher Cu^0 concentration (Fig. 2). Mg10 is believed to have the highest Cu^0 fraction due to its strong visible light absorption. Notably, Cu^{2+} could not be the primary Cu state in glass when Cu^0 particles were abundantly present, as revealed by

the opaque red (also called "ruby") color of glass Mg10 [33]. Therefore, Cu^0 with a low Cu^+ concentration was assumed to be the primary Cu state in glass Mg10. The average valence of Cu from the glasses could change in the following order: Mg10 (Cu^0 with small Cu^+) < Ca10 ≈ Sr10 (Cu^+ with small Cu^0) < Base (Cu^+) < Ba10 (Cu^+ with small Cu^{2+}).

The pyrolysis of the precursor $NH_4H_2PO_4$ during the melting of glass batches produced NH_3, which could possibly reduce Cu^{2+} from precursor CuO into Cu^+ and Cu^0 above 400 °C [34]. However, during temperature elevation in glass melting, the decreased viscosity of the glass melts could facilitate the exhaustion of NH_3 and the dissolution of O_2 from the air, which could oxidize Cu^+ and Cu^0 into Cu^{2+} and Cu^+, respectively [34]. The base glass had a higher average Cu valence than Ca10, but the base glass melt had a higher viscosity with slower exhaustion of NH_3 (Fig. 7). Consequently, this could be attributed to the inhibited growth of the Cu^0 particles due to the fast cooling of the glass melts, leading to the absence of absorbance of the Cu^0 particles for the base glass in the UV-vis spectrum (Fig. 2). Therefore, to favor the Cu^0 growth, Base-S, Ca10-S, and Ba10-S glasses were prepared with the same compositions as the base, Ca10, and Ba10 glasses following the same routes, but the glass melts naturally cooled down in the air instead of being manually pressed by a brass plate for fast cooling (Table 1, Section 2.1). All the naturally cooling samples showed a deep opaque red color, accompanied by distinct SPR peaks of Cu^0 around 570 nm for Base-S and Ba10-S (which were absent for the fast cooling Base and Ba10 glasses in Fig. 2) and a strong light absorbance of this peak for Ca10-S (which displayed moderate absorbance for the fast cooling Ca10 glass in Fig. 2), as shown in Fig. 8. This indicated increased concentrations of Cu^0 particles for all the naturally cooling samples. The concentration of Cu^0 particles could further increase when the Base-S, Ca10-S, and Ba10-S glasses were remelted under the N_2 atmosphere due to the increased absorbance of the Cu^0 colloidal particles near 600 nm (Fig. 8) and the enhanced Cu^0 diffraction peak (Fig. 9). When the Base-S, Ca10-S, and Ba10-S glasses were remelted in the air, the decreased absorbance of the Cu^0 colloidal particles in all three glasses and the presence of the absorption Cu^{2+} band near 780 nm in glass Ba10-S were attributed to

the oxidation of Cu^{+}/Cu^{0} through O_2 consumption from the air (Fig. 8). Glass Ba10-S had a stronger oxidation effect on the Cu species than glass Base-S, indicating that the redox properties of the atmosphere during glass melting could more profoundly influence the Cu species dispersed in glass Ba10-S with a lower viscosity (Fig. 7). Additionally, the higher viscosity of the base glass could inhibit the Cu^{0} diffusion to retard the growth of the Cu^{0} particles, leading to a colorless optical appearance of the base glass (Fig. 2).

4.2. Evolution of glass structure

4.2.1. Phosphorus-oxygen network

The depolymerization of the phosphorus-oxygen network structure was evident when MgO was introduced into the base glass due to decreased Q^2 and increased Q^1 units (Fig. 4 and Table 3). The conversion from Q^2 into Q^1 units was slightly enhanced when a lower field strength AE replaced MgO, indicative of depolymerization of the phosphorus-oxygen network. The fractions of Q^2 and Q^1 units are dependent on the molar ratios O/P and can be calculated based on compositions of glasses as shown in [35]. However, assuming that all the Cu was incorporated into the glass network as Cu^{2+}, the glasses Mg10, Ca10, and Ba10 have higher actual fraction of Q^2 units (Table 3) analyzed by NMR fitting than the theoretical fraction calculated by the analyzed composition based on ICP-AES techniques. As discussed in section 4.1, the dispersing of Cu^{0} was recorded in the naturally cooling glasses Ca10-S and Ba10-S, which indicated that the AE-containing glasses Mg10, Ca10, and Ba10 could contain amounts of Cu^{0} in their glass system. This could lead to less incorporation of the copper ions into the phosphorus-oxygen network, resulting in the higher actual fraction of Q^2 units. Moreover, the chemical shifts of Q^1 and Q^2 gradually increased as the AE field strength decreased. This uniform behavior showed that the M^{2+} cations could interact with the Q^1 and Q^2 units, indicating their random distribution between the short chains (Q^2) [32]. However, the FWHM of Q^2 in glasses gradually increased from 12.9 to 15.0 ppm as the AE field strength reduced, revealing that the broadening of the peaks increased the disorder from the distributions of P-O bond lengths and O-P-O and P-O-P bond angles [32].

The depolymerized phosphorus-oxygen networks led to a loose glass structure, potentially deteriorating the aqueous durability. However, the glasses with additional AE had normalized concentrations of release for all elements below ~1.5 g/L, significantly lower than ~6.5 g/L in the base glass, indicating improved water resistance of the glasses (Fig. 5b). This could be attributed to the increased crosslinks provided by the additional AE, which reduced susceptibility to hydrolysis and decreased solubility [11]. Moreover, substituting a lower field strength cation for a higher cation like Ca^{2+} for Mg^{2+} could form a less covalent, hydration-resistant bonding with the phosphate terminal oxygens, which increased the hydration kinetics of the phosphate chains tied together by the lower field strength cations in earlier studies [8][14]. Unexpectedly, these substitutions peculiarly decreased the normalized concentrations of the elements leached out from the glass, which suggested enhanced water resistance of glass despite the similar polymerization of the phosphorus-oxygen network and the decreased field strength of the additional AE (Fig. 5b and Table 3).

4.2.2. Zn coordination

As ZnO acted as another major component with 45–50 mol% content in the glasses, the local Zn structure could significantly impact the glass structure and properties. The EXAFS spectral profiles of Zn K-edge in *R*-space showed a sharp feature centered at ~1.6 Å, which corresponded to the first coordination of Zn in the base glass (Fig. 10a). This feature shifted to a lower radial distribution when AE was introduced, revealing a decreased atomic distance of Zn-O.

The analysis of the EXAFS spectral profiles in *k*-space obtained the curve-fitting parameters: coordination number (*N*), atomic distances (*R*), and Debye-Waller factors (σ^2) of Zn-O coordination in glasses (Table 4, Fig. 10b). In agreement with previous studies, *N* was estimated at ~4.3 for the base glass [15][36]. The *N* value increased to > 4.8 with the addition of AE, which might compensate for the increased terminal oxygen atoms from the short chains shown in Figs. 3 and 4, as explicated in the report [1]. As shown in Table 4, a higher *N* generally correlated with a lower σ^2, indicating reduced vibrational amplitudes and improved structural stability of Zn-O coordination [37]. The improved structural stability of Zn-O coordination and the introduced AE

could potentially lead to a less open glass structure for the AE-containing glasses, which improved the water resistance (Fig. 5b) and was in agreement with previous studies [11][38][39].

4.3. Dissolution behavior of glass

The dissolution behavior of the different AE-containing glasses as functions of aqueous immersion duration was used to study the release behavior of antibacterial agents Cu and Zn, which significantly determined their long-term antibacterial activity (Fig. 11). The relative content of phosphorus ion represents the mass percentage of phosphorus ion in the leachate relative to that in 0.50 g of glass powders, where the relative contents of zinc, alkaline earth (M), or copper ion were acquired using the same method. The base glass released around 83% of P to the leachate within 0.5 d, followed by gradually reduced P concentration in the leachate (Fig. 11a). The relative content of zinc ions in the leachate displayed the same behavior as a function of time, but the highest value was below 60% (Fig. 11b). The decreased phosphorus and zinc ion concentrations in the leachate originated from precipitation, as explicated in the literature [8]. Additionally, glass Mg10 showed a similar burst dissolution behavior but at a slower rate. The relative contents of phosphorus and zinc ions in the leachate reached their highest values within 4–8 d, at around 60% and 40%, respectively, and concurrently decreased about 20% in 73 d. Glasses Ca10 and Sr10 demonstrated nearly identical dissolution behavior as Mg10, indicating that the small change of glass structure led to limited alteration of the long-term dissolution behavior of glasses with different additions of Mg, Ca, and Sr.

Glass Ba10 had an extremely slow dissolution behavior compared to the other three AE-containing glasses, but the Ba10 glass structure displayed limited change as shown in Figs. 3, 4, and 10. The relative contents of all ions from glass Ba10 in the leachate slightly increased and were below 4.5% within 8 d. The relative contents of phosphorus and zinc ions were suddenly increased to around 20% in 16 d and turned into a steady behavior with the immersion time prolonged to 33 d. The dissolution of glass Ba10 resumed when the time increased to 73 d. Notably, the relative content of barium ions in the leachate was below 3% and 9% within 8 and 33 d, respectively, lower

than that of phosphorus and zinc ions in Ba10 (Fig. 11c).

The morphological evolutions of Ca10 and Ba10 glasses during immersion were characterized using FE-SEM to investigate the anomalous dissolution behavior of glass Ba10. At 2 and 16 d, the Ca10 surface was rough and alteration products with the shape of irregular flaky particles were seen attached to the glass (Figs. 12a and b). When the time reached 50 d, a porous alteration layer with a rough surface was formed on the glass surface. The alteration products were comprised of crystallized zinc phosphate hydrates, as examined using XRD patterns in Fig. 13. As shown in Figs. 12d–f, a thin and dense layer with thickness below 200 nm was formed on the Ba10 glass surface and a rough morphology was observed under the thin layer within 2–50 d, accompanied by a low released concentration of elements compared to that from other glasses shown in Fig. 11. This phenomenon was analogous to the durable borosilicate and aluminophosphate glasses used for nuclear waste vitrification [40][41]. As shown in Fig. 14d, the Ba/P and Ba/Zn atomic ratios increased from around 0.10 to 0.26 and from around 0.28 to 0.52 as a function of time, respectively, which indicated that Ba dissolved more slowly into the leachate compared with P and Zn in the glass Ba10 and was in agreement with the lower concentration of Ba in the leachate, as shown in Fig. 11c. Additionally, this layer, where Ba was a major component, was assumed to be unstable and prone to water-induced degradation, inducing the resumption of glass dissolution after 8 d of aqueous immersion.

Among the four AE, Ba had the weakest field strength due to its largest ionic radius, which could produce less covalent and hydration-resistant bonds with the phosphate terminal oxygens and increased the hydration kinetics, as explicated in the study of Brow [42]. However, incorporating Ba^{2+} or Pb^{2+}, which acted as larger cations with lower field strength compared to Mg^{2+} and Ca^{2+}, into the binary glass with a molar composition $60P_2O_5$-$40Fe_2O_3$ displayed higher aqueous durability, as discussed in the study of Bingham [12]. The weak field strength of Ba^{2+} resulted in a low polarization of the terminal oxygen atoms at the phosphate chain binding sites, which interacted weakly with water [43][44]. Consequently, this led to slow disruptions of ionic crosslinks from Ba^{2+} between P-O chains and a decreased Ba release rate from the glass

matrix.

On the other hand, the relationships between modifier ion properties and phosphate glass durability are not well understood, but it seems clear that the simple field strength arguments are quite inadequate as discussed in [12]. The large size of Ba could inhibit the diffusion of ions during glass dissolution, resulting in a limited alteration and well-improved water resistance [10]. Besides, the structure of Ba^{2+} in the glass system might be similar to that in the crystals such as $Ba_2P_2O_7$ with an extremely low solubility in water, leading to the slow dissolution behavior in the initial stage. However, the effect of the thin and dense layer on the dissolution behavior of glass was unclear despite characterizations using FE-SEM and XPS. Hence, the composition, structure, and formation mechanism of this layer require further investigations in the following studies.

5. Conclusions

AE with increasing field strengths was incorporated into Cu-doped zinc metaphosphate glass to promote the oxidation of Cu^0/Cu^+ into Cu^+/Cu^{2+}, which was induced by the accelerated exhaustion of NH_3 at the glass melting stage and the dissolution of O_2 due to the decreased viscosity of the melts. Due to the accumulation of crosslinks, the increased ionic valence states Cu^+/Cu^{2+} could increase the network bonding and connectivity of glass. Despite the depolymerization of the phosphorus-oxygen network, the incorporation of AE into the glass system enhanced the water resistance through the introduction of divalent cations that provided the crosslink in the glass network and possible through the improved structural stability of Zn-O coordination. Notably, a thin and dense layer was formed on the Ba10 glass surface during immersion, accompanied by a relatively lower elemental release. This thin layer could have a passivation role in improving the long-term water resistance and long-lasting antibacterial activity of glass Ba10.

Acknowledgements

The authors gratefully acknowledge the project of Science and Technology Plan (Grant No. 2022CX006) from Chuzhou government. The authors thank Dr. Hanyu Hu from Université Paris-Saclay, CEA, France for suggestions on the analysis of NMR results.

Reference

[1] Y. Xia, H. Chen, I. Hung, Z. Gan, S. Sen, Structure and Fragility of Zn-phosphate glasses: Results from multinuclear NMR spectroscopy and calorimetry, Journal of Non-Crystalline Solids. 580 (2022) 121395. https://doi.org/10.1016/j.jnoncrysol.2022.121395.

[2] S. Mokhtari, K.D. Skelly, E.A. Krull, A. Coughlan, N.P. Mellott, Y. Gong, R. Borges, A.W. Wren, Copper-containing glass polyalkenoate cements based on SiO_2-ZnO-CaO-SrO-P_2O_5 glasses: glass characterization, physical and antibacterial properties, Journal of Materials Science. 52 (2017) 8886–8903. https://doi.org/10.1007/s10853-017-0945-5.

[3] F.N.S. Raja, T. Worthington, L.P.L. Souza, S.B. Hanaei, R.A. Martin, Synergistic antimicrobial metal oxide-doped phosphate glasses; a potential strategy to reduce antimicrobial resistance and host cell toxicity, ACS Biomaterials Science & Engineering. 8 (2022) 1193–1199. https://doi.org/10.1021/acsbiomaterials.1c00876.

[4] F. Barba, P. Callejas, Calcium phosphate silicate ceramics for heavy metal immobilization and antibacterial activity in waste water, Journal of Materials Science. 41 (2006) 5227–5230. https://doi.org/10.1007/s10853-006-0440-x.

[5] Y. Onodera, S. Kohara, H. Masai, A. Koreeda, S. Okamura, T. Ohkubo, Formation of metallic cation-oxygen network for anomalous thermal expansion coefficients in binary phosphate glass, Nature Communications. 8 (2017) 15449. https://doi.org/0.1038/ncomms15449.

[6] A. Obata, D. S. Brauer, T. Kasuga, Phosphate and borate bioactive glasses, Biomaterials Science Series No. 11. The Royal Society of Chemistry, London, 2022.

[7] J. Massera, K. Bourhis, L. Petit, M. Couzi, L. Hupa, M. Hupa, J.J. Videau, T. Cardinal, Effect of the glass composition on the chemical durability of zinc-phosphate-based glasses in aqueous solutions, Journal of Physics and Chemistry of Solids. 74 (2013) 121–127. http://dx.doi.org/10.1016/j.jpcs.2012.08.010.

[8] B.C. Bunker, G.W. Arnold, J.A. Wilder, Phosphate glass dissolution in aqueous solutions, Journal of Non-Crystalline Solids. 64 (1984) 291–316. https://doi.org/10.1016/0022-3093(84)90184-4.

[9] G. Navarra, A. Falqui, G. Piccaluga, G. Pinna, The structure of a zinc metaphosphate glass. A reverse Monte Carlo study, Physical Chemistry Chemical Physics. 4 (2002) 4817–4822. https://doi.org/10.1039/b204964c.

[10] S. Li, H. Liu, F. Wu, Z. Chang, Y. Yue, Effects of alkaline-earth metal oxides on structure and properties of iron phosphate glasses, Journal of Non-Crystalline Solids. 434 (2016) 108–114. http://dx.doi.org/10.1016/j.jnoncrysol.2015.12.004.

[11] N. Kanwal, H. Toms, A. C. Hannon, F.A. Perras, D.L. Bryce, N. Karpukhina, I. Abrahams, Structure and solubility behaviour of zinc containing phosphate glasses, Journal of Materials Chemistry B. 3 (2015) 8842–8855. http://dx.doi.org/10.1039/c4tb01504e.

[12] P.A. Bingham, R.J. Hand, O.M. Hannant, S.D. Forder, S.H. Kilcoyne, Effects of modifier additions on the thermal properties, chemical durability, oxidation state and structure of iron phosphate glasses, Journal of Non-Crystalline Solids. 355 (2009) 1526–1538. https://doi.org/10.1016/j.jnoncrysol.2009.03.008.

[13] S. Lee, F. Nagata, K. Kato, T. Nakano, T. Kasuga, Structures and dissolution behaviors of quaternary CaO-SrO-P_2O_5-TiO_2 glasses, Materials. 14 (2021) 1736–1748. https://doi.org/10.3390/ma14071736.

[14] J.C. Knowles, K. Franks, I. Abrahams, Investigation of the solubility and ion release in the glass system K_2O-Na_2O-CaO-P_2O_5, Biomaterials. 22 (2001) 3091–3096. https://doi.org/10.1016/S0142-9612(01)00057-6.

[15] R.K. Brow, D.R. Tallant, S.T. Myers, C.C. Phifer, The short-range structure of zinc polyphosphate glass, Journal of Non-Crystalline Solids. 191 (1995) 45–55. https://doi.org/10.1016/0022-3093(95)00289-8.

[16] M. Vincent, P. Hartemann, M. Engels-Deutsch, Antimicrobial applications of copper, International Journal of Hygiene and Environmental Health. 219 (2016) 585–591. http://dx.doi.org/10.1016/j.ijheh.2016.06.003.

[17] T.M. Gross, J. Lahiri, A. Golas, J. Luo, F. Verrier, J.L. Kurzejewski, D.E. Baker, J. Wang, P.F. Novak, M.J. Snyder, Copper-containing glass ceramic with high antimicrobial efficacy, Nature Communications. 10 (2019) 1979–1987. https://doi.org/10.1038/s41467-019-09946-9.

[18] P. Colomban, A. Tournié, P. Ricciardi, Raman spectroscopy of copper nanoparticle-containing glass matrices: ancient red stained-glass windows, Journal of Raman Spectroscopy. 40 (2009) 1949–1955. https://doi.org/10.1002/jrs.2345.

[19] J.A.Duffy, Redox equilibria in glass, Journal of Non-Crystalline Solids. 196 (1996) 45–50. https://doi.org/10.1016/0022-3093(95)00560-9.

[20] G. Fang, C. Liu, K. Li, K. Xu, X. Zhao, Vitrification of nuclear-contaminated HEPA filter media: A study on the viscosity-component correlation and the volatilization of simulated radionuclides, Journal of Non-Crystalline Solids. 619 (2023) 122568. https://doi.org/10.1016/j.jnoncrysol.2023.122568.

[21] Q. Qin, N. Stone-Weiss, N. Shi, P. Mukherjee, J. Ren, A. Goel, Synergy between Ca^{2+} and high ionic field-strength cations during the corrosion of alkali aluminoborosilicate glasses in hyper-alkaline media, Journal of the American Ceramic Society. 107 (2024) 7153–7174. https://doi.org/10.1111/jace.19806.

[22] O. Soriano-Romero, R. Lozada-Morales, A.N. Meza-Rocha, S. Carmona-Tellez, U. Caldino, B. Flores-Desirena, R. Palomino-Merino, Cold bluish white and blue emissions in Cu^{+}-doped zinc phosphate glasses, Journal of Luminescence. 217 (2020) 116791–116798. https://doi.org/10.1016/j.jlumin.2019.116791.

[23] J.A. Jimenez, Efficient stabilization of Cu^{+} ions in phosphate glasses via reduction of Cu^{2+} by Sn^{2+} during ambient atmosphere melting, Journal of Materials Science. 49 (2014) 4387–4393. https://doi.org/10.1007/s10853-014-8138-y.

[24] A. Goldstein, M. Vulfson, M. Sirota. Optical spectra of copper-doped Zn-phosphate glasses, Journal of the American Ceramic Society. 90 (2007) 3680–3682. https://doi.org/10.1111/j.1551-2916.2007.01959.x.

[25] J. Gao, R. Ma, J. Zhao, Q. Xu, X. Qiao, J. Du, X. Fan, Non-bridging oxygen dependent redox and spectroscopic properties of Cu species in phosphosilicate glasses, Journal of Alloys and Compounds 664 (2016) 331–337. http://dx.doi.org/10.1016/j.jallcom.2015.12.041.

[26] B. Qian, X. Lian, C. Wang, S. Yang, Structure and properties of calcium iron phosphate glasses, Journal of Nuclear Materials. 443 (2013) 140–144. http://dx.doi.org/10.1016/j.jnucmat.2013.07.014.

[27] L. Zhang, R.K. Brow, M.E. Schlesinger, L. Ghussn, E.D. Zanotto, Glass formation from iron-rich phosphate melts, Journal of Non-Crystalline Solids. 356 (2010) 1252–1257. https://doi.org/10.1016/j.jnoncrysol.2010.04.019

[28] G.L. Saout, P. Simon, F. Fayon, A. Blin, Y. Vaills, Raman and infrared study of $(PbO)_x(P2O5)_{(1-x)}$ glasses, Journal of Raman Spectroscopy. 33 (2002) 740–746. https://doi.org/10.1002/jrs.911.

[29] Z. Černošek, S. Brázdová, J. Holubová, Binding possibilities of calcium, zinc and copper in metaphosphate glasses a more detailed study, Journal of Non-Crystalline Solids. 546 (2020) 120264. https://doi.org/10.1016/j.jnoncrysol.2020.120264.

[30] G. Tricot, Insertion of Al_2O_3 in Zinc Metaphosphate Glasses: New Insights from 1D/2D Solid State NMR, The Journal of Physical Chemistry C. 125 (2021) 9210–9218. https://doi.org/10.1021/acs.jpcc.0c10723.

[31] R.J. Kirkpatrick, R.K. Brow, Nuclear magnetic resonance investigation of the structures of phosphate and phosphate-containing glasses: a review, Solid State Nuclear Magnetic Resonance. 5 (1995) 9–21. https://doi.org/10.1016/0926-2040(95)00042-O.

[32] U. Hoppe, A. Saitoh, T. Shimizu, G. Tricot, A.C. Hannon, Properties and structure of ternary BaO-SnO-P2O5 glasses, Journal of Non-Crystalline Solids. 597 (2022) 121909. https://doi.org/10.1016/j.jnoncrysol.2022.121909.

[33] S. Banerjee, A. Paul, Thermodynamics of the System Cu-0 and Ruby Formation in Borate Glass, Journal of the American Ceramic Society. 57 (1974) 286–290. https://doi.org/10.1111/j.1151-2916.1974.tb10902.x.

[34] N. Wada, J. Hanai, M. Furukawa, K. Kojima, Preparation of Mn^{2+}-Cu^{+} co-doped P_2O_5-ZnO-Al_2O_3 glasses and their red fluorescence properties, Journal of the American Ceramic Society. 102 (2019) 4621–4631. https://doi.org/10.1111/jace.16302.

[35] R. Hussin, D. Holland, R. Dupree, A MASNMR structural study of cadmium phosphate glasses, Journal of Non-Crystalline Solids 298 (2002) 32–42. https://doi.org/10.1016/S0022-3093(01)01049-3.

[36] M. Bionducci, G. Licheri, A. Musinu, G. Navarra, G. Piccaluga, and G. Pinna, The Structure of a Zn(II) Metaphosphate Glass. I. The Cation Coordination by a Combination of X-Ray and Neutron Diffraction, EXAFS and X-Ray Anomalous Scattering, Zeitschrift für Naturforschung A. 51 (1996) 1209–1215. https://doi.org/10.1515/zna-1996-1211.

[37] X.C. Yang, M. Dubiel, S. Brunsch, H. Hofmeister, X-ray absorption spectroscopy analysis of formation and structure of Ag nanoparticles in soda-lime silicate glass, Journal of Non-Crystalline Solids. 328 (2003) 123–136. https://doi.org/10.1016/S0022-3093(03)00469-1.

[38] X. Li, H. Yang, X. Song, Y. Wu, Glass forming region, structure and properties of zinc iron phosphate glasses, Journal of Non-Crystalline Solids. 379 (2013) 208–213. http://dx.doi.org/10.1016/j.jnoncrysol.2013.08.014.

[39] S. Li, Y. Lu, Y. Qu, Y. Xu, L. Ming, Z. Song, Y. Yue, Influences of ZnO on the chemical durability and thermal stability of calcium iron phosphate glasses, Journal of Non-Crystalline Solids. 498 (2018) 228–235. https://doi.org/10.1016/j.jnoncrysol.2018.06.023.

[40] S. Gin, X. Beaudoux, F. Angéli, C. Jégou, N. Godon, Effect of composition on the short-term and long-term dissolution rates of ten borosilicate glasses of increasing complexity from 3 to 30 oxides, Journal of Non-Crystalline Solids. 358 (2012) 2559–2570. https://doi.org/10.1016/j.jnoncrysol.2012.05.024.

[41] P.P. Poluektov, O.V. Schmidt, V.A. Kascheev, M.I. Ojovan, Modelling aqueous corrosion of nuclear waste phosphate glass, Journal of Nuclear Materials. 484 (2017) 357–366. https://doi.org/10.1016/j.jnucmat.2016.10.033.

[42] E. Metwalli, R. K. Brow, Modifier effects on the properties and structures of aluminophosphate glasses, Journal of Non-Crystalline Solids. 289 (2001) 113–122. https://doi.org/10.1016/S0022-3093(01)00704-9.

[43] M. Itadani, G. Tricot, B. Doumert, H. Takebe, A. Saitoh, Structure and properties of barium tin boro-phosphate glass systems with very low photoelastic constant, Journal of Applied Physics. 122 (2017) 085102. http://dx.doi.org/10.1063/1.4998957.

[44] J. Cha, T. Kubo, H. Takebe, M. Kuwabara, Compositional dependence of properties of SnO-P_2O_5 glasses, Journal of the Ceramic Society of Japan. 11 (2008) 915–919. https://doi.org/10.2109/jcersj2.116.915.

Table 1. Nominal composition of the glass hosts. All samples were additionally added with 2 mol% CuO. The nominal molar ratio of O/P were 3.02 for the base glass and 3.13 for the AE-containing glasses. The volatilization of P_2O_5 (in the parenthesis), actual molar content of Al_2O_3 (in mol%), and molar ratio of O/P were retained using ICP-AES.

Sample	Composition (mol%)						Analyzed	
	P_2O_5	ZnO	MgO	CaO	SrO	BaO	Al_2O_3	O/P
Base	50 (−1.3%)	50	/	/	/	/	0.42	3.05
Mg10	45 (−1.2%)	45	10	/	/	/	0.43	3.17
Ca10	45 (−4.7%)	45	/	10	/	/	0.62	3.22
Sr10	45 (−0.4%)	45	/	/	10	/	0.70	3.17
Ba10	45 (−2.2%)	45	/	/	/	10	0.77	3.19

Table 2. Raman band assignments and the related Q^n units. Q and n represent the phosphorus-oxygen tetrahedron and the number of BO in each tetrahedron, respectively.

Raman shift (cm^{-1})	Raman assignments
702	POP_{sym} stretch (bridging oxygen), Q^2 units
758	POP_{sym} stretch (bridging oxygen), Q^1 units
1010	P-O stretch, Q^1 chain terminator
1048	$(PO_3)_{sym}$ stretch (nonbridging oxygen), Q^1 units
1138	P-O stretch, Q^1 chain terminator
1185–1206	$(PO_2)_{sym}$ stretch (nonbridging oxygen), Q^2 units
1252	$(PO_2)_{asym}$ stretch (nonbridging oxygen), Q^2 units

Table 3. ^{31}P NMR parameters: Chemical shift (δ_{iso}, ± 0.1 ppm), full width at half-maximum (FWHM, ± 0.2 ppm) and proportions (prop., ± 2%). The deviations of Q^2 fraction between fitting results analyzed by NMR and theoretical results analyzed by ICP-AES were shown in the bracket. For instance, the fitting result on Q^2 fraction of the base glass was 89.3%, 1.5% lower than the theoretical result 90.8%.

Sample	Q^1			Q^2		
	δ_{iso}/ppm	FWHM/ppm	prop./%	δ_{iso}/ppm	FWHM/ppm	prop./%
Base	–12.4	10.2	10.7	–30.7	12.9	89.3(−1.5%)
Mg10	–13.0	12.4	25.9	–30.6	13.4	74.1(6.0%)
Ca10	–11.7	11.6	34.7	–29.2	14.2	65.3(6.4%)
Sr10	–11.2	11.0	31.7	–28.5	14.6	68.3(−0.7%)
Ba10	–11.0	10.7	29.8	–28.2	15.0	70.2(5.3%)

Table 4. Coordination number (N), atomic distance (R) and Debye-Waller factors (σ^2) of zinc-oxygen coordination in glasses, along with R-factors showing the validity of fitting.

Sample	N	R/Å	σ^2/Å^2	R-factor
Base	4.3 (5)	1.94	0.014 (3)	0.008
Mg10	4.8 (7)	1.93 (7)	0.007 (2)	0.014
Sr10	4.9 (4)	1.94 (7)	0.008 (1)	0.006
Ba10	5.0 (6)	1.94 (7)	0.008 (2)	0.019

Note: The atomic distance for the base glass was cited from [36]. Values in parentheses represent errors of the last digit.

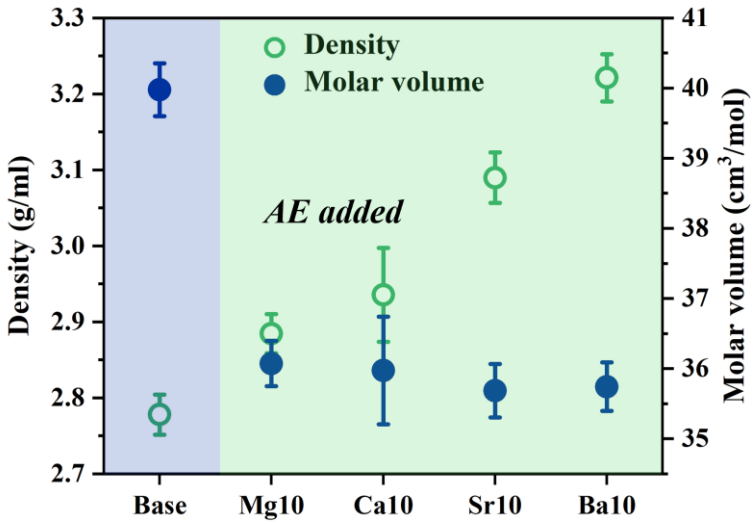

Fig. 1 Density and molar volume (V_m) of the base glass and different AE-containing glasses.

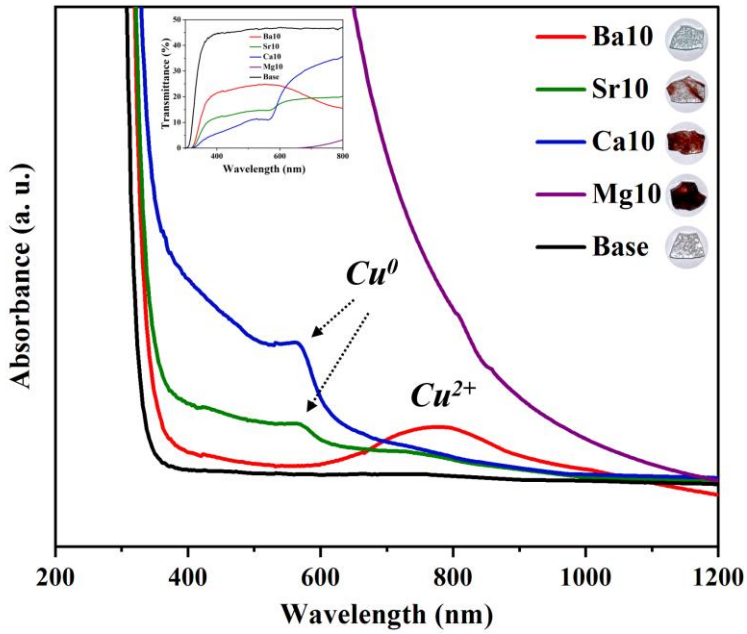

Fig. 2 Images and optical absorption spectra of the base glass and different AE-containing glasses. The inset figure shows the transmittance of glasses.

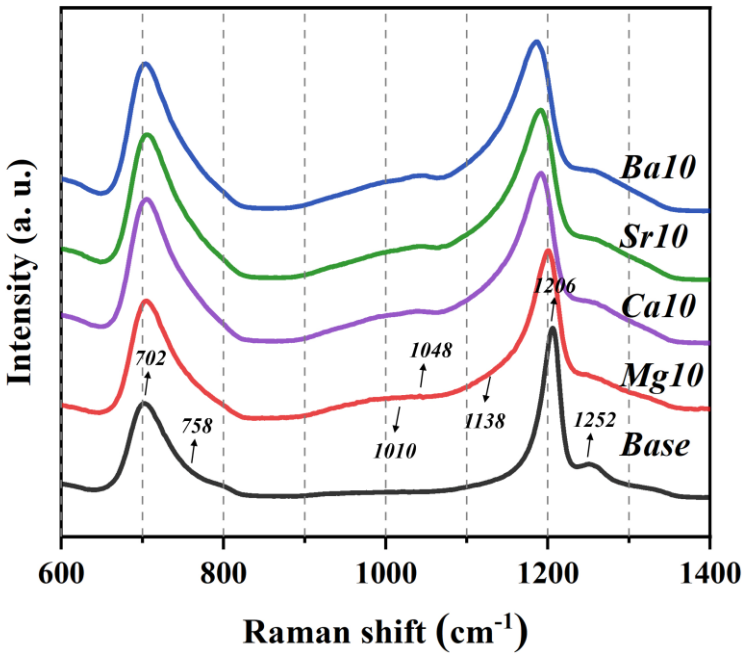

Fig. 3 Raman spectra of base glass and different AE-containing glasses.

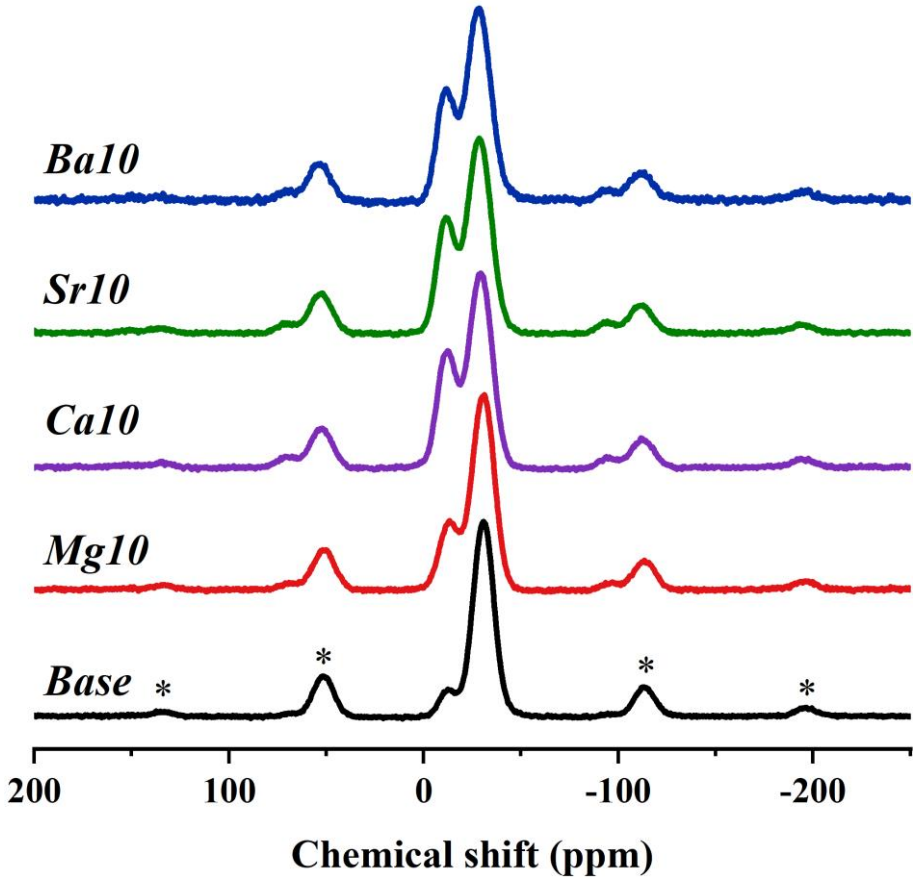

Fig. 4 ^{31}P NMR spectra of the base glass and different AE-containing glasses. The star label represents the spinning sidebands.

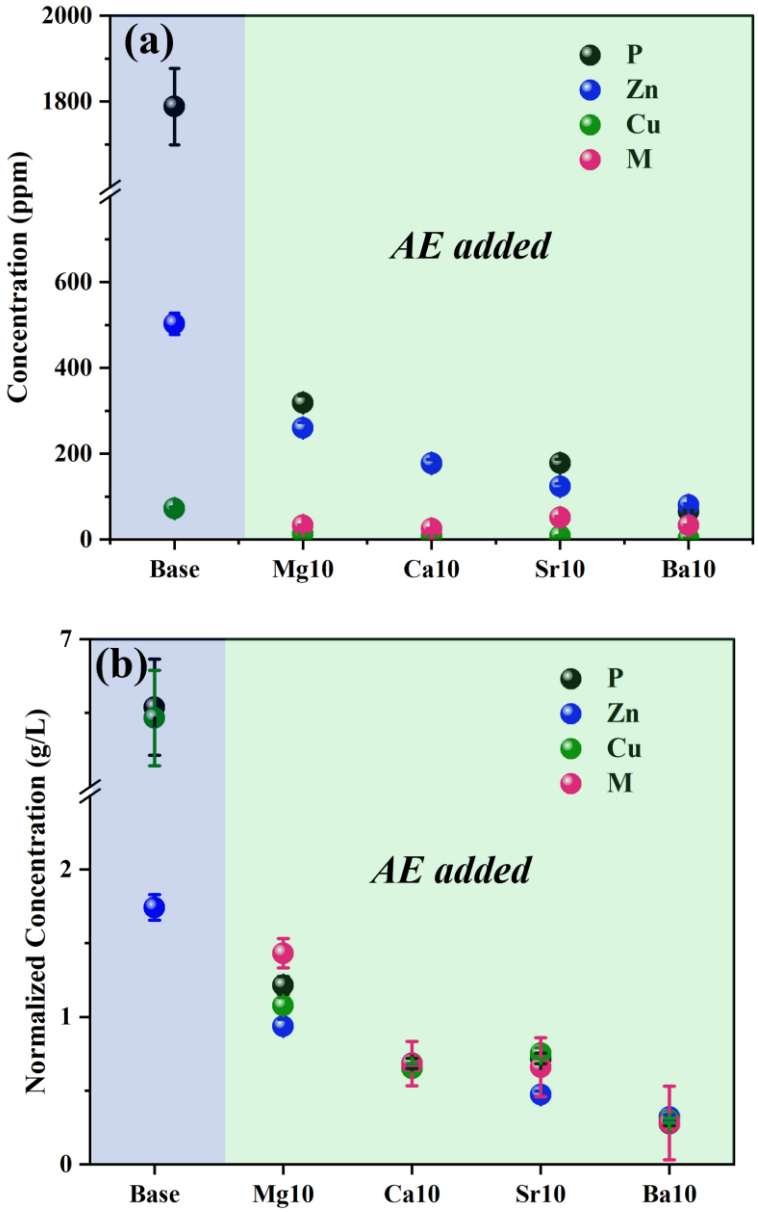

Fig. 5 (a) Elemental and (b) normalized elemental concentrations in leachates after 2 h of immersion for the base glass and different AE-containing glasses. M represented alkaline earth metal elements.

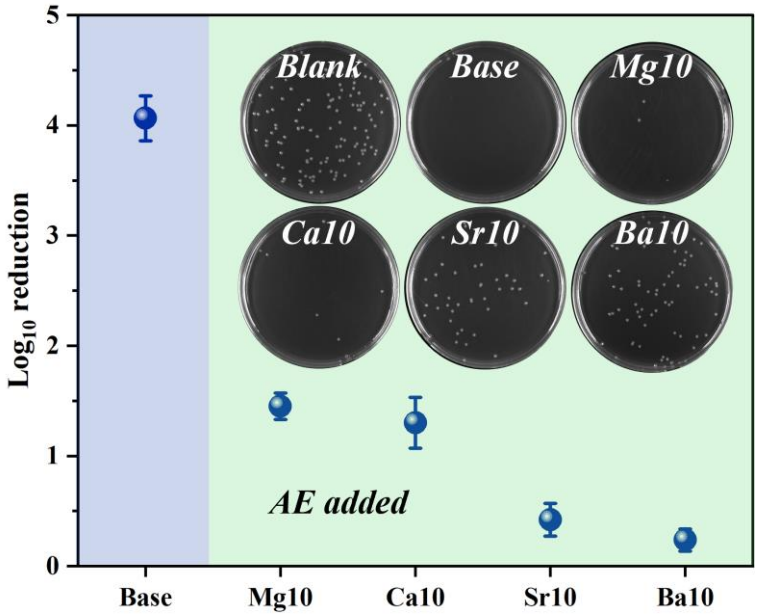

Fig. 6 Images of the bacterial colonies and bacterial reduction of the base glass and different AE-containing glasses.

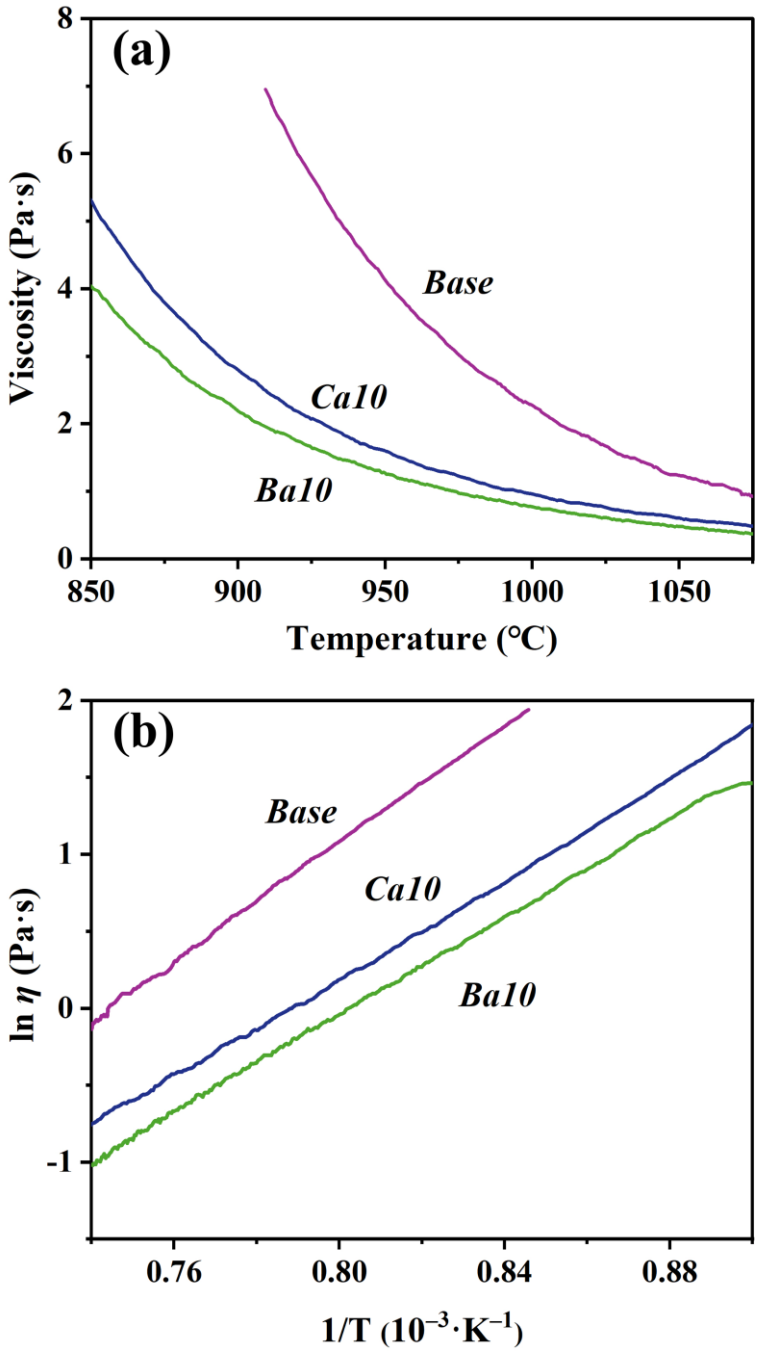

Fig. 7 For the Base, Ca10, and Ba10 glasses (a) viscosity (η) versus temperature and (b) ln η as functions of 1/T ($10^{-3}\cdot K^{-1}$). The Arrhenius equation well represented the linear curves indicating the viscosity–temperature relationship.

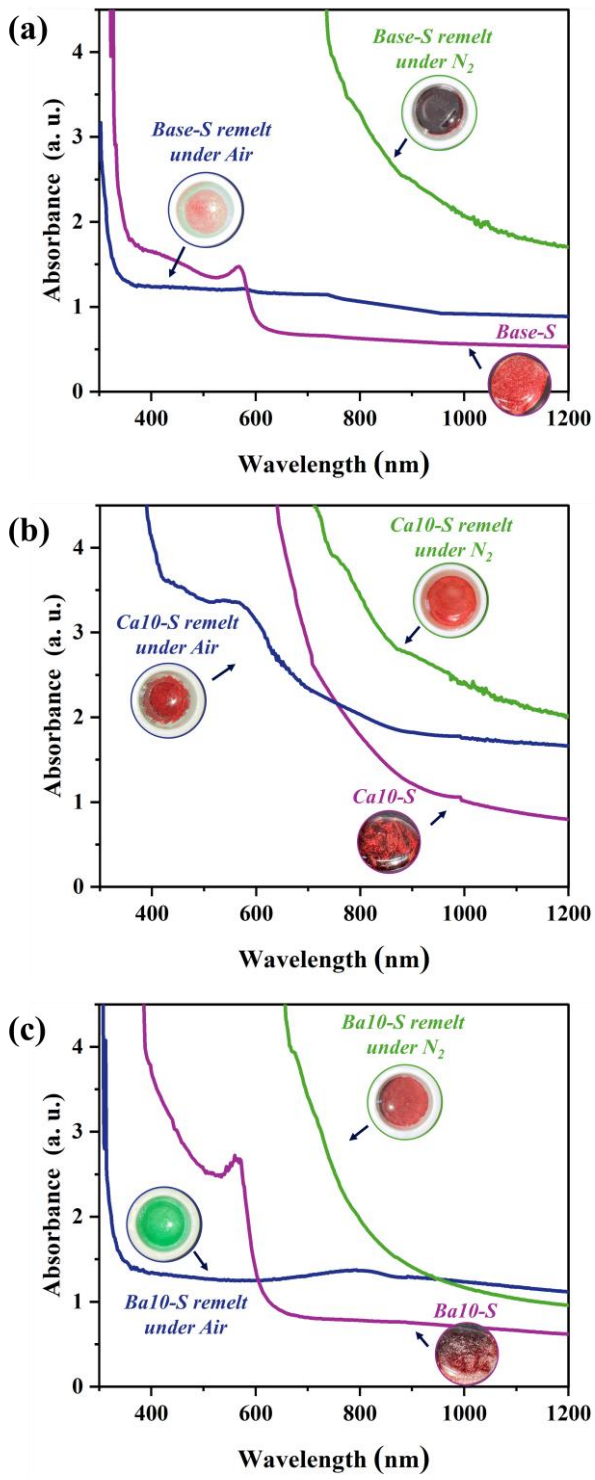

Fig. 8 Images and optical absorption spectra of (a) Base-S glass (prepared by naturally cooling the glass melt on a preheated brass plate) and its remelt under the air and N_2, (b) Ca10-S glass and its remelt under the air and N_2, and (c) Ba10-S glass and its remelt under the air and N_2.

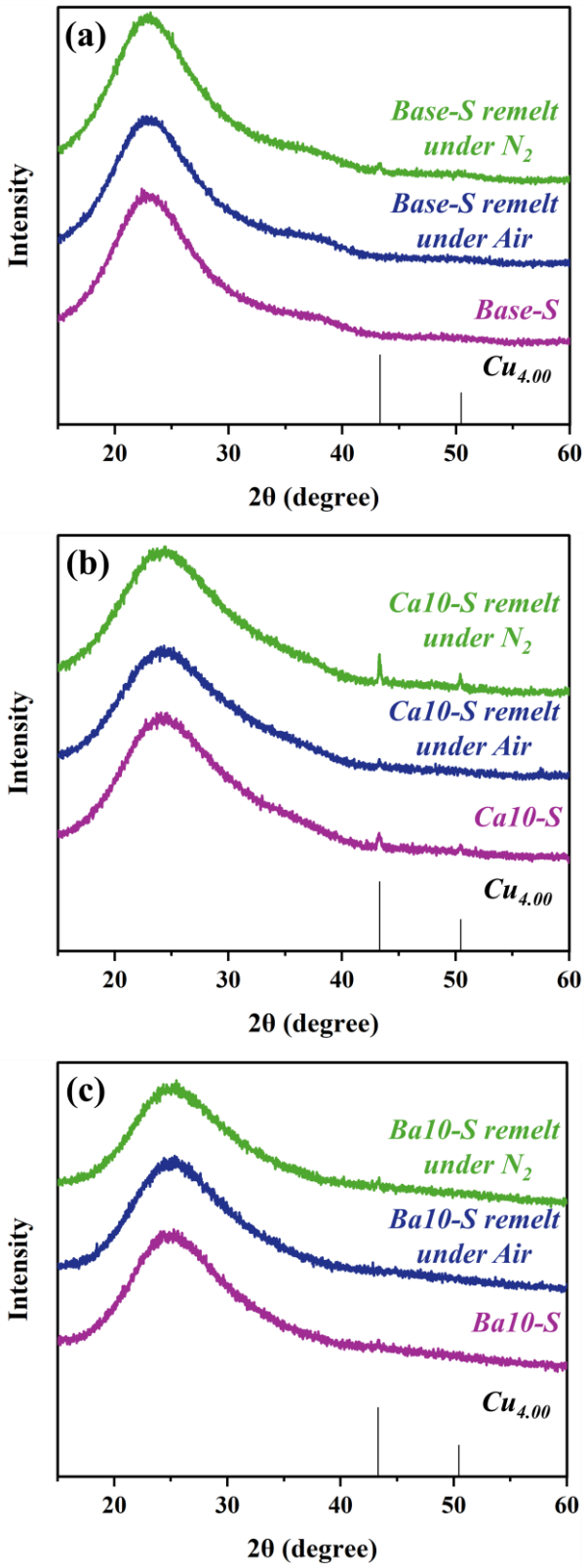

Fig. 9 XRD spectra of the glasses and their remelts. (a) Base-S, (b) Ca10-S, and (c) Ba10-S. The reference code of $Cu_{4.00}$ is 96-901-2044.

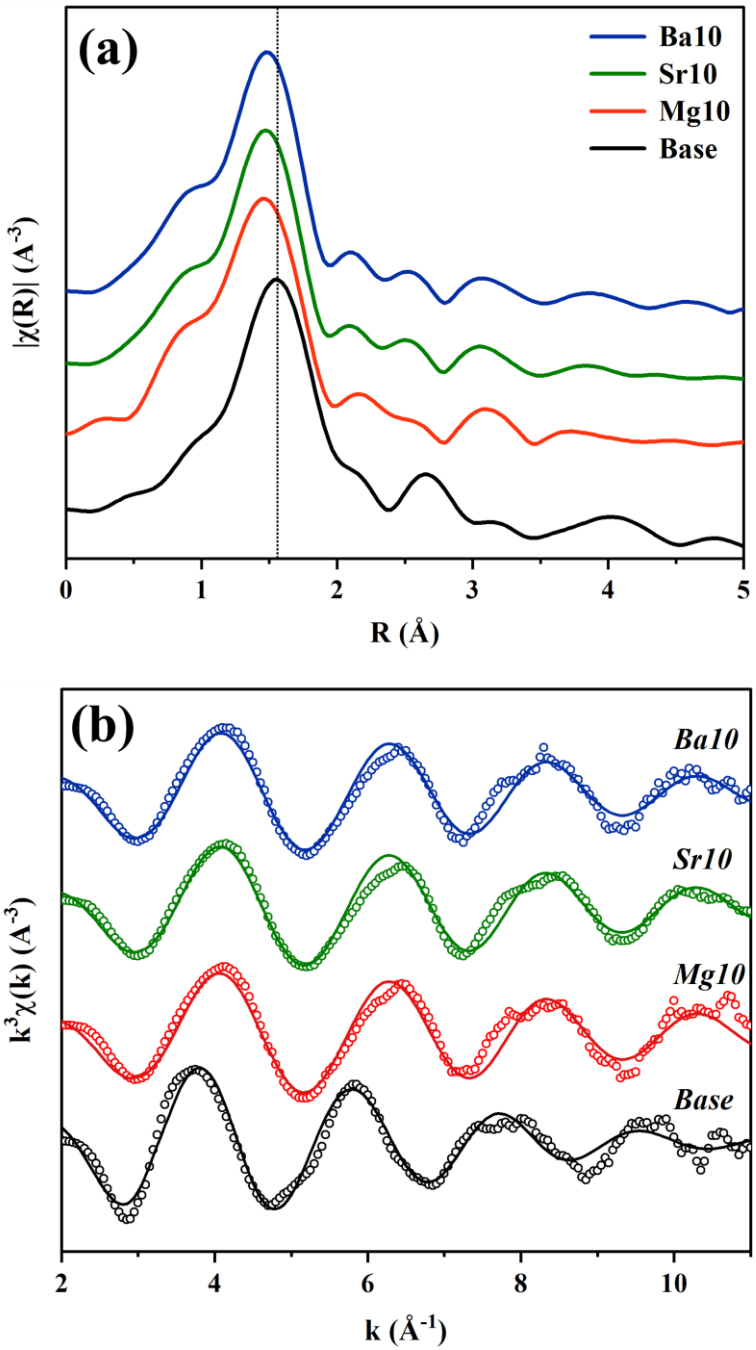

Fig. 10 The EXAFS spectra of base glass and different AE-containing glasses. (a) The Fourier transform of Zn K-edge EXAFS spectra in the *R*-space of the Base, Mg10, Sr10, and Ba10 glasses. The dotted line is a reference line to analyze the radial distribution shift of different glasses. (b) Zn K-edge EXAFS spectra in the *k*-space of the Base, Mg10, Sr10, and Ba10 glasses. Experimental data, hollow dot, and theoretical fit, line.

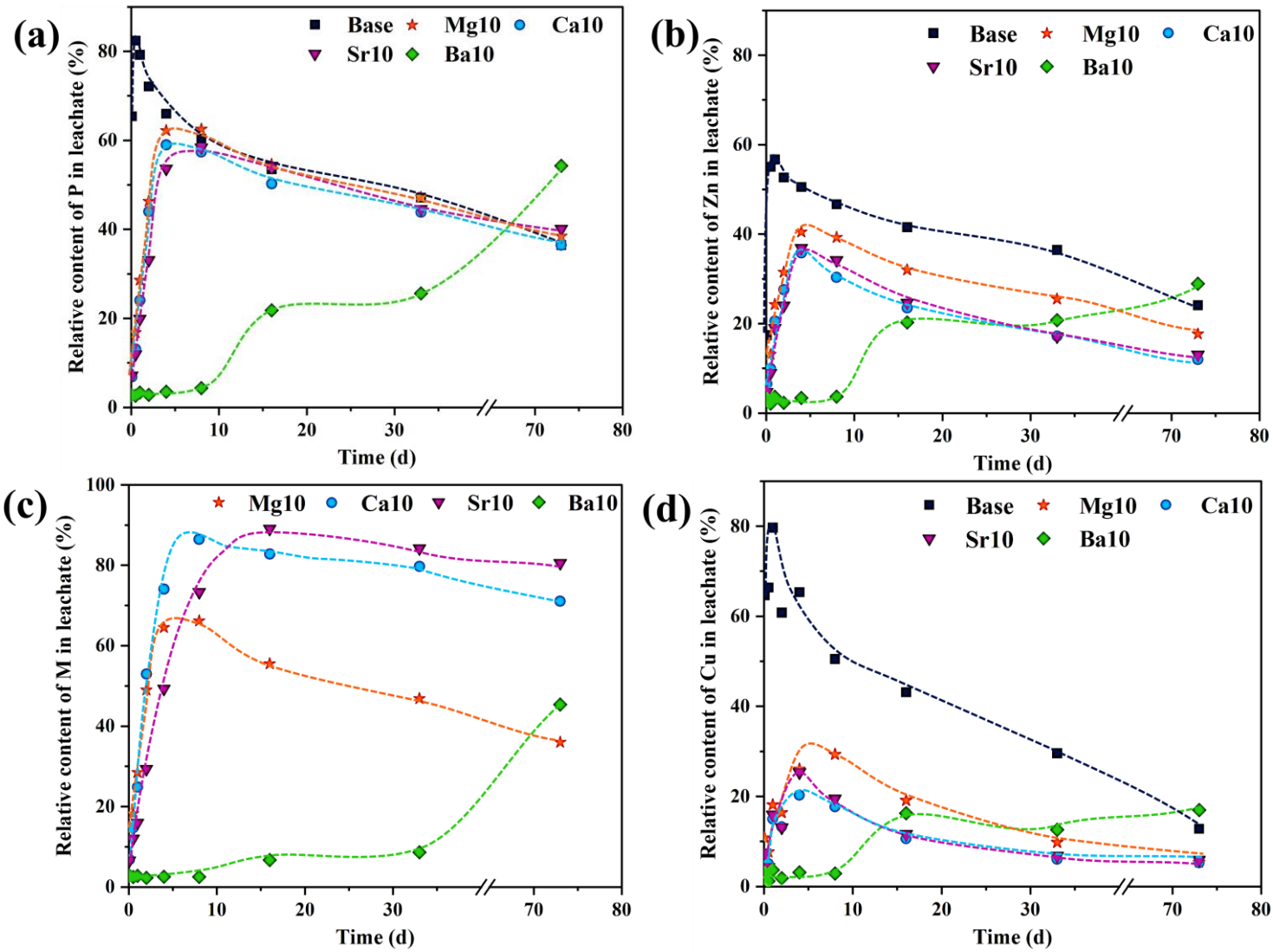

Fig. 11 The relative contents of the ions of (a) phosphorus, (b) zinc, (c) alkaline earth (M), and (d) copper in ultrapure water as a function of the immersion time. Data errors are estimated below 10%, and error bars are hidden for better visualization. The dashed lines represent trend lines.

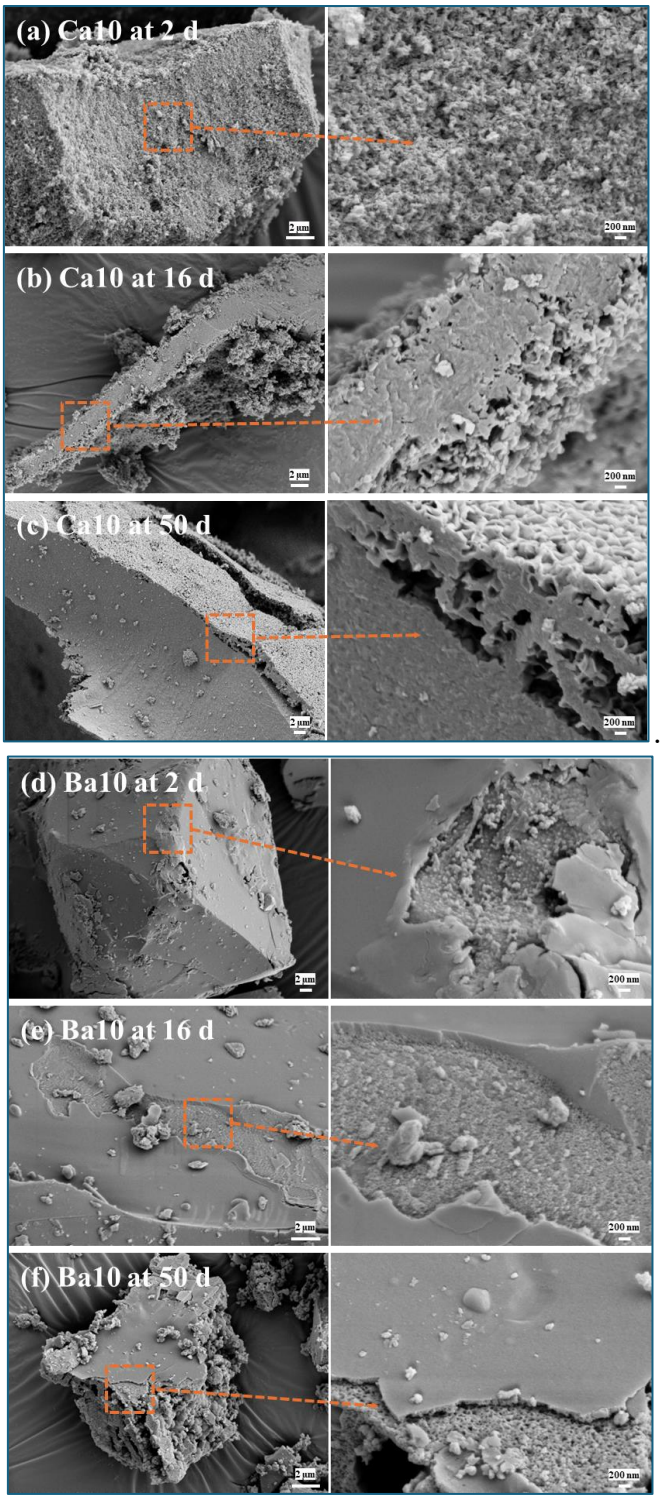

Fig. 12 The FE-SEM images of Ca10 glass after immersion in ultrapure water for (a) 2, (b) 16, and (c) 50 d. The FE-SEM images of Ba10 glass after immersion in ultrapure water for (d) 2, (e) 16, and (f) 50 d. The figures on the right side represent the magnification of Figures (a–f).

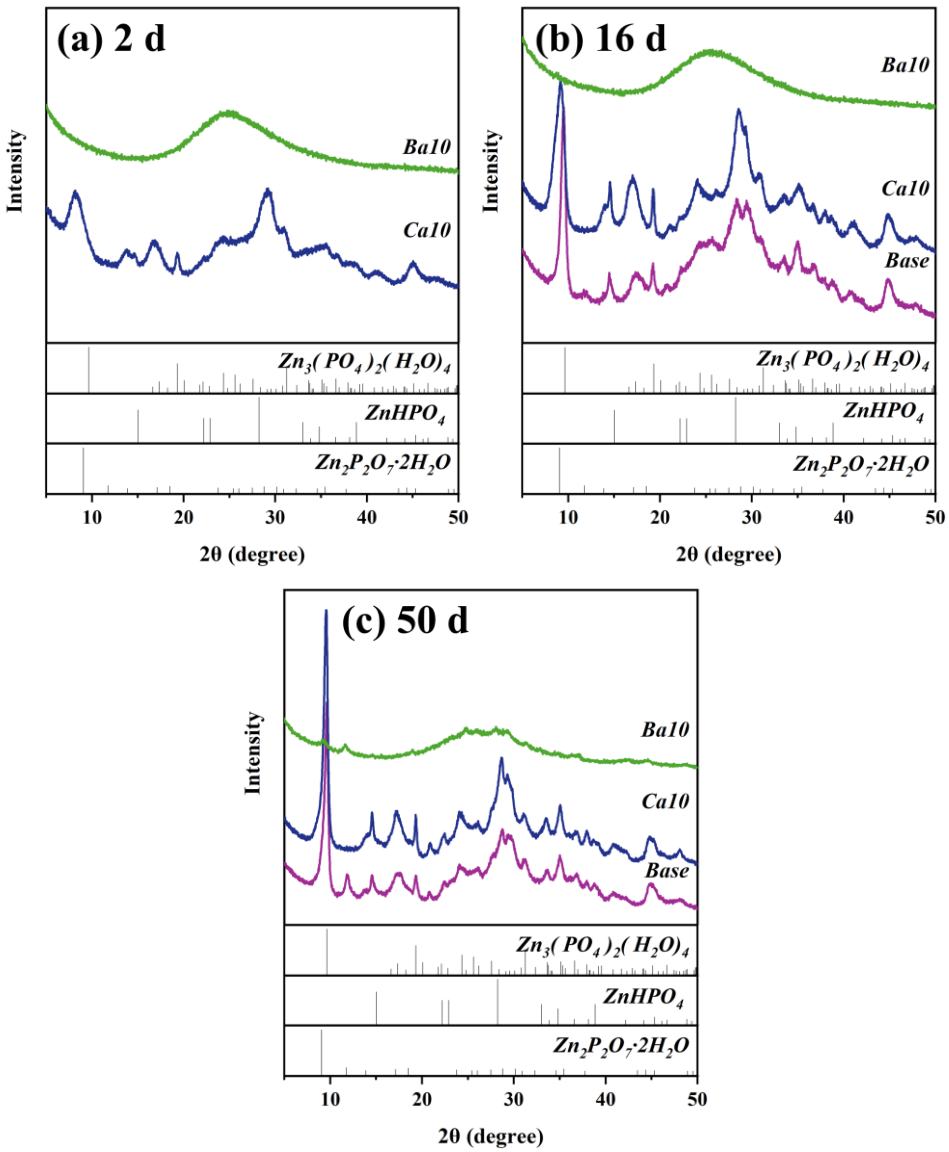

Fig. 13 XRD patterns of the Base, Ca10, and Ba10 glasses after immersion in ultrapure water for (a) 2, (b) 16, and (c) 50 d. The reference codes of $Zn_3(PO_4)_2(H_2O)_4$, $ZnHPO_4$, and $Zn_2P_2O_7{\cdot}2H_2O$ are 01-074-2275, 00-039-0708, and 00-044-0769, respectively.

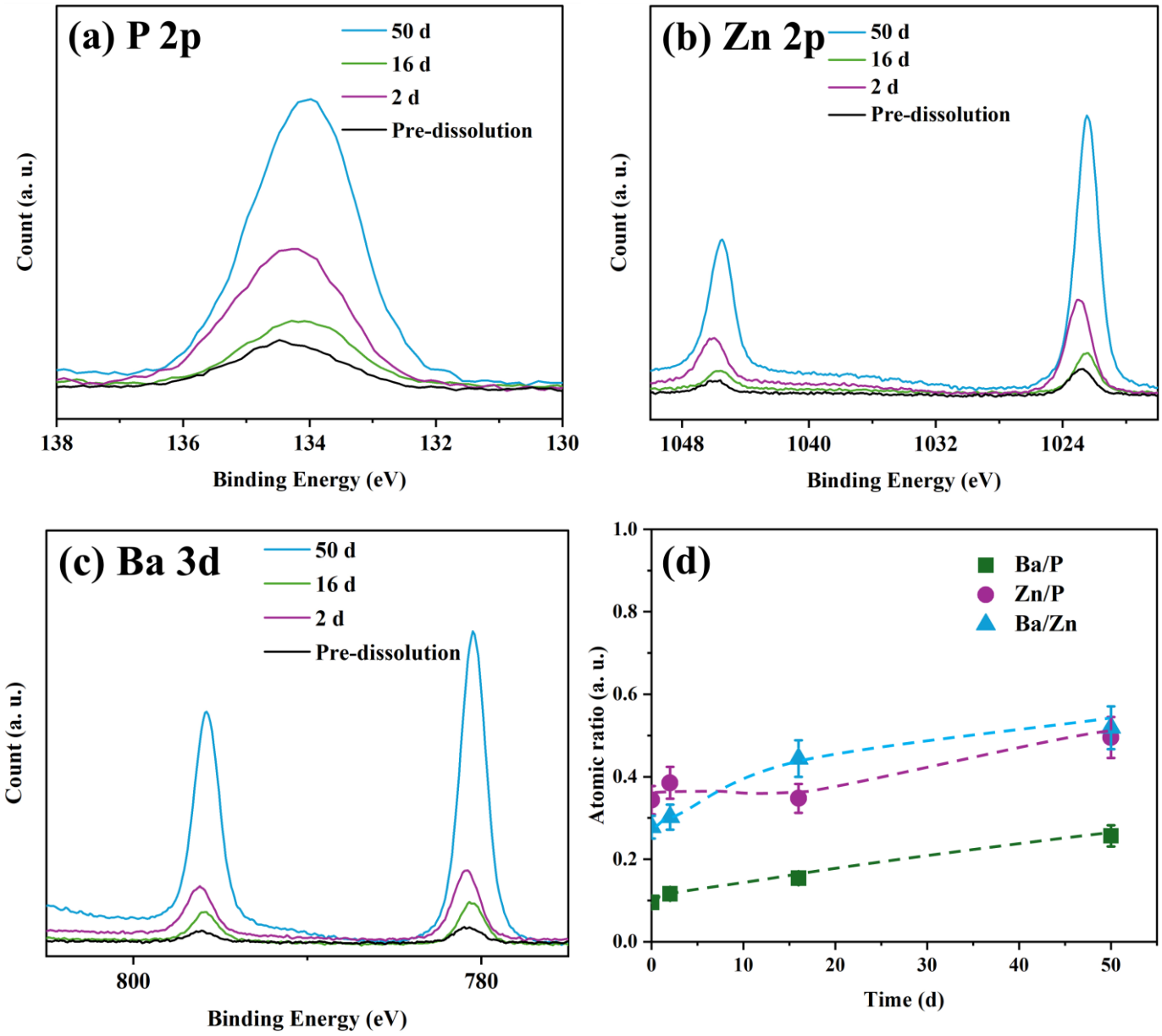

Fig. 14 The XPS core-level spectra of (a) P 2p, (b) Zn 2p, and (c) Ba 3d measured on the top ~5–10 nm of the Ba10 glass surface before and after immersion in ultrapure water for 2, 16, and 50 d. (d) The atomic ratio calculated of Ba10 glass as a function of the immersion time using XPS analysis.